Properties of small-scale Alfvén waves and accelerated electrons from FAST

C. C. Chaston, J. W. Bonnell, C. W. Carlson, and J. P. McFadden
Space Sciences Laboratory, University of California, Berkeley, California, USA

R. E. Ergun
Laboratory for Atmospheric and Space Physics, University of Colorado, Boulder, Colorado, USA

R. J. Strangeway
Institute for Geophysical and Planetary Physics, University of California, Los Angeles, California, USA

Received 28 March 2002; revised 18 August 2002; accepted 18 October 2002; published 18 January 2003.

[1] The FAST spacecraft observes Alfvénic fluctuations in field quantities throughout the auroral oval. In this report, we show preliminary results from a statistical study of Alfvén waves with transverse scales comparable to the electron skin-depth observed over the frequency range from 0.2 to ~20 Hz in the spacecraft frame. This study shows that these waves are most commonly found in the magnetospheric cusps and at the polar cap boundary of the auroral oval in the premidnight sector where the most intense events are observed. It is shown that the wave Poynting flux is well correlated with the energy flux of field-aligned upgoing and downgoing electrons. It is also shown that over the FAST altitude range (350–4175 km), the wave Poynting flux decreases with decreasing altitude, most likely due to losses through electron acceleration. It is demonstrated, however, through the use of simulations and observations that most of the electron acceleration occurs at altitudes above FAST between 1 and 2 Earth radii (R_E), with the most energetic electrons arriving from an altitude of ~2–3 R_E for statistically determined density and composition profiles. *INDEX TERMS:* 2704 Magnetospheric Physics: Auroral phenomena (2407); 2431 Ionosphere: Ionosphere/magnetosphere interactions (2736); 2716 Magnetospheric Physics: Energetic particles, precipitating; 2736 Magnetospheric Physics: Magnetosphere/ionosphere interactions

Citation: Chaston, C. C., J. W. Bonnell, C. W. Carlson, J. P. McFadden, R. E. Ergun, and R. J. Strangeway, Properties of small-scale Alfvén waves and accelerated electrons from FAST, *J. Geophys. Res.*, *108*(A4), 8003, doi:10.1029/2002JA009420, 2003.

1. Introduction

[2] Alfvén waves carry significant energy flux into the auroral oval [*Wygant et al.*, 2000]. They provide a direct means for energy transport into this region from processes occurring on the boundaries of the Earth's magnetosphere. Much of this incoming electromagnetic energy is converted to particle kinetic energy in the form of accelerated electrons. The means by which this occurs was first postulated by *Hasegawa* [1976] and *Goertz and Boswell* [1979] who demonstrated that Alfvén waves with scales perpendicular to the geomagnetic field ($\mathbf{B}_o$) of the order of the ion acoustic gyroradius or electron inertial length could carry an electric field parallel to $\mathbf{B}_o$.

[3] Subsequent to the development of these theories there have been numerous reported observations of small-scale Alfvén waves above the auroral oval. *Dubinin et al.* [1985] using observations from ICB-1300 revealed Alfvénic structures at altitudes of 850 km with perpendicular scales of a few kilometers at frequencies in the spacecraft frame of order ~1 Hz [*Chmyrev et al.*, 1988]. *Boehm et al.* [1990] showed from rocket observations a correlation between Alfvénic structures on these scales, accelerated electrons and density depressions. Observations from the Freja spacecraft [*Louarn et al.* 1994; *Wahlund et al.*, 1994] showed these waves occurred on highly dissipative perpendicular scales, were often solitary wave like and revealed an association between Alfvén waves and broadband ELF emissions. *Volwerk et al.* [1996] estimated the field-aligned Poynting flux in these waves and showed that this is similar to that expected for typical energy fluxes for accelerated electrons observed in the auroral oval. It was later shown that these emissions were strongly correlated with ion-heating [*Knudsen and Wahlund*, 1998]. These results and others are presented in a review of observations of small-scale Alfvén waves above the auroral oval by *Stasiewicz et al.* [2000].

[4] Most recently observations [*Wygant et al.*, 2000] from the Polar spacecraft at 4–6 R_E above the Earth have shown large Alfvén wave Poynting fluxes in the plasma sheet boundary layer directed Earthward along auroral fieldlines which correlate with bright aurora at the magnetic footprint in the auroral ionosphere. At altitudes below 1 R_E observa-

0148-0227/03/2002JA009420$09.00

tions from FAST show a one to one correlation between the appearance of Alfvén waves and bursts of field aligned and Earthward streaming electrons [*Chaston et al.*, 1999a, 2001]. Similar observations are reported at lower altitudes from rockets [*Ivchenko et al.*, 1999] and from the Freja spacecraft [*Knudsen et al.*, 1998; *Koyaintsev et al.*, 2000; *Andersson et al.*, 2002]. Conjunction studies from ground based observations of aurora and spacecraft measurements of Alfvén waves have verified the association between electron acceleration in Alfvén waves and visible auroral emissions [*Lotko et al.*, 1998; *Hallinan et al.*, 2001].

[5] Simulation results have shown how efficiently Alfvén waves in the inertial limit may accelerate electrons [*Thompson and Lysak*, 1996; *Kletzing*, 1994; *Hui and Seyler*, 1992] to account for observed electron energy and pitch angle distributions [*Chaston et al.*, 2000a, 2003a]. Alfvén waves then clearly play a role in electron acceleration above the aurora but how are these events distributed throughout the oval, what does this distribution tell us about the sources of these waves, and do we observe decreases in wave Poynting flux consistent with increases in electron energy flux over the altitude range traversed by the FAST spacecraft? It is the intention of this report to address these questions by first examining the properties of Alfvénic wave events as functions of MLT, ILAT and altitude and second from simulations where appropriate.

[6] This paper is organized as follows: In section 2 we present a case study example and justify the selection of the frequency range used; in section 3 we define the database of Alfvén wave events derived from the data; in section 4 we briefly discuss the relationship between the observed waves and observed auroral forms, in section 5 we examine the distribution of wave and electron properties as functions of MLT and invariant latitude; in section 6 we consider the relationship between electron and wave energy flux (Poynting flux); in section 7 we examine the altitude dependency of the wave and electron properties; in section 8 we discuss the observations in terms of the predictions from simulations of a propagating inertial Alfvén wave in the auroral plasma and the possible sources for these waves; then in section 9 we summarize the findings of this study and conclude.

2. Spacecraft Frame Wave Frequency and Structuring of Electron Precipitation

2.1. Event Overview

[7] Figure 1 shows an example of an Alfvén wave event in the premidnight polar cap boundary. Panel a) shows the magnetic field ($B_{\perp 2}$) measured perpendicular to the spacecraft trajectory and B_o or roughly in a direction tangential to the auroral oval boundary. This field quantity is composed of fluctuations over a range of frequencies from 50 mHz to greater than 1 Hz. Fluctuations above ~20 Hz are removed by the recursive magnetometer filter however these can be studied from the induction magnetometer results (which we will discuss later). Panel b) shows the electric field ($E_{\perp 1}$) measured along the spacecraft trajectory and also perpendicular to B_o. This direction is roughly perpendicular to the polar cap boundary. The interval of turbulence in this component is well correlated with that of the magnetometer.

[8] Panels c) and d) of Figure 1 show the electron energy and pitch angle spectra. These panels reveal bursts of field-aligned (0°) electrons coincident with the wave activity at energies mostly less than 5 keV with the most energetic burst extending up to 10 keV (or roughly up to the energy of the plasma sheet electrons). The plasma sheet component can be seen as the faint band at several keV that begins at the far left of panel c) and provides the isotropic background fluxes shown in the pitch angle spectra. The small energy fluxes and the absence of a sharp low energy cutoff in this component suggest that there is no significant field-aligned potential drop (i.e. no "inverted-V") above the spacecraft in this region.

[9] Brief bursts of counter field-aligned (180°) electrons are occasionally observed (at 2022:47 UT for example) throughout the displayed interval with energies less than 100 eV. These are distinct from the backscattered field-aligned electrons present throughout the display interval (which span the full width of the loss cone) since their fluxes are considerably larger than that of the backscatter and are even more field-aligned than the downgoing electrons. Furthermore there is a dropout of field-aligned fluxes just prior to their observation.

[10] Panel e) contains the integrated electron energy flux in the source cone populated by the field-aligned electron bursts and shows that these electrons supply up to 45 mW m^{-2} of electron energy flux into the ionosphere. These fluxes are sufficient to cause bright aurora [*Chaston et al.*, 2003b]. The gray line in this panel is the approximate field-aligned wave Poynting flux calculated from $E_{\perp 1}$ and $B_{\perp 2}$ (which statistically [*Stasiewicz et al.*, 2000] are the largest amplitude components of the observed E and B wave fields). This quantity due to its spiky nature appears largely uncorrelated with the electron energy flux except for the largest peaks at 2022:55 UT and 2022:46 UT. It will however be shown in section 2.2 that at frequencies in the spacecraft frame less than ~2 Hz a correlation well above that expected for noise exists.

[11] Panels f) and g) show the ion measurements over this time interval. The period of wave activity is coincident with enhanced fluxes of upstreaming ions with energies generally less than 1 keV distributed as conics at angles very close to 90/270° suggestive of near local heating. Integrated fluxes at this time are up to 10^9 cm^{-2} s^{-1}. Ion outflow in this region has been studied previously by *Tung et al.* [2001] who show that these ions provide a significant contribution to ions of ionospheric origin populating the plasma sheet. While the main purpose of this work is to examine electron acceleration in Alfvén waves we have included these ion spectra since it will become apparent later in this report that these heated ions may play an active role in Alfvén wave damping over the FAST altitude range.

2.2. Frequency Space Analysis

[12] To determine the frequency range in the spacecraft frame most appropriate for comparing wave and electron energy flux observations we perform wavelet transforms of the wave field and electron data. We choose a Morlet basis function in this case since the waveforms we observe are often far from sinusoidal but rather appear as packets or wave bursts over a range of frequencies in the electric field extending well above the oxygen gyro frequency [*Wahlund*

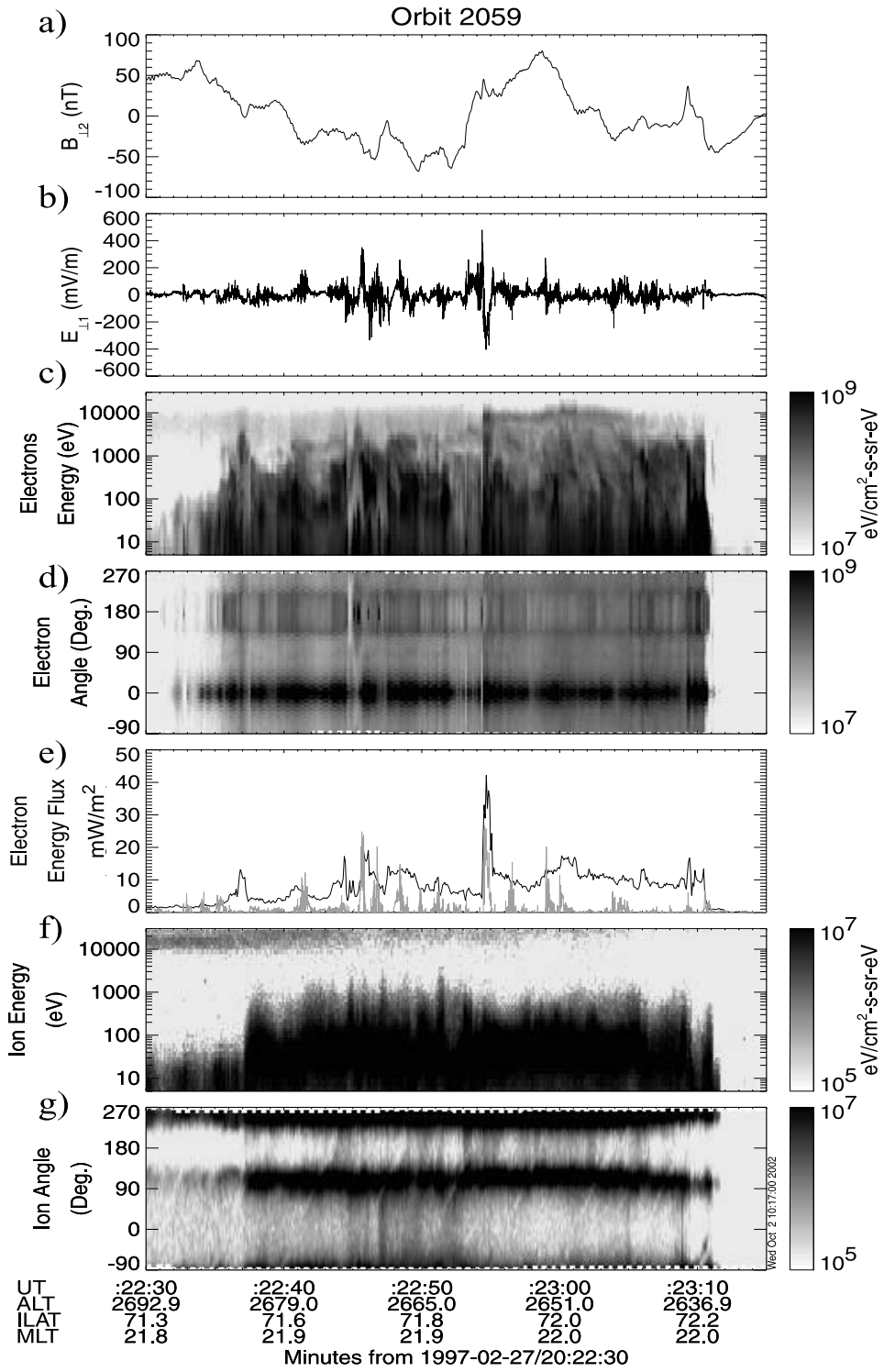

Figure 1. Case study Alfvén wave observations on the polar cap boundary. Panel a) shows the wave magnetic field, $B_{\perp 2}$, measured perpendicular to the geomagnetic field B_o and roughly in the east-west direction. Panel b) shows the wave electric field, $E_{\perp 1}$, measured in quadrature to $B_{\perp 2}$ and B_o. Panel c) shows the electron energy spectra. Panel d) shows the electron pitch angle spectra with 0° downward. Panel e) shows the integrated electron energy flux in the source cone mapped to the ionosphere (at 100 km altitude). The gray trace in this panel is the field-aligned wave Poynting flux also mapped to the ionosphere. Panel f) shows the ion energy spectra and panel g) shows the ion pitch angle spectra.

et al., 1994] (Ω_{O+}) which is $\sim 20 \times 2\pi$ rads^{-1} at this altitude. Figure 2a shows the averaged wavelet transform of the ratio of the wave magnetic field amplitude ($B_{\perp 2}$) to the wave electric field amplitude ($E_{\perp 1}$) normalized in terms of the local Alfvén speed ($V_A = 1.3 \times 10^7$ ms^{-1}) over the interval shown in Figure 1. In preparing this spectrum we have used measurements from both the fluxgate (solid line) and induction magnetometers (dashed line) flown on the FAST spacecraft. For the sampling frequency of the fluxgate magnetometer at this time the recursive filter sets a corner in the spectrum at 5.45 Hz clearly visible in the spectral result (for some sampling modes this is at 21.8 Hz). Above this frequency we are reliant on the induction coil results, which can be seen to smoothly replace the fluxgate results at this frequency. The Alfvén speed in this case has been determined from the electron density indicated by the emissions at the electron plasma frequency and from the mass spectrometer experiment which gives a reliable indication of composition in regions such as these where intense ion conics are observed [*Tung et al.*, 2001].

[13] It is assumed that field fluctuations with ($B_{\perp 2}/E_{\perp 1}$)V_A values from 0.1 to 10 and wave frequencies less than the local oxygen cyclotron frequency are Alfvénic. Based on this criteria, Figure 2a indicates that the waves observed can be identified as "Alfvénic" over the frequency range in the spacecraft frame from $\sim$0.2 Hz up to $\sim$20 Hz. In fact over most of this range we find that ($B_{\perp 2}/E_{\perp 1}$)V_A is relatively flat with a value just above 1 or slightly more magnetic than expected for an ideal propagating Alfvén wave. Figure 2b shows the averaged wavelet transform of the wave electric ($E_{\perp 1}$) and magnetic ($B_{\perp 2}$) fields that were used to create Figure 2a. The $E_{\perp 1}$ (dark line) spectrum reveals a peak at $\sim$0.5 Hz which extends to the low frequency end of the "Alfvénic" range identified in Figure 2a. The $B_{\perp 1}$ spectra (gray lines) is more power law like throughout the "Alfvénic" range so that at frequencies less than the 0.5 Hz peak in $E_{\perp 1}$, the wave becomes more magnetic than an ideal MHD Alfvén wave. Above this frequency the electric and magnetic field spectra decrease together maintaining ($B_{\perp 2}/E_{\perp 1}$)$V_A \sim 1$.

[14] The frequency limits of this "Alfvénic" range are in part imposed by observational constraints. The most significant of these is the difficulty associated with separating spatial and temporal variations in the spacecraft frame. In Figure 2a it can be seen that ($B_{\perp 2}/E_{\perp 1}$)V_A has a value close to 1 at frequencies above the oxygen gyro frequency (the upper boundary of the "Alfvénic" frequency range) with the wave not becoming increasingly electrostatic until above 40 Hz. Since the perpendicular phase speed of these waves can be expected to be less than the spacecraft speed [*Stasiewicz et al.*, 2000] it is likely that much of the time dependency observed in the spacecraft frame is due to spacecraft Doppler shift. Due to the electron inertial correction, for small enough perpendicular wavelengths, even those more electrostatic features above 40 Hz (and up to the 100 Hz limit shown here) may interpreted as Alfvénic with the observed wave frequency Doppler shifted above Ω_{O+}. However, without resorting to interferometric techniques the identification of the wave mode cannot be certain. The correct identification of the wave is necessary since in the plasma frame the dispersion of waves approaching and above the oxygen cyclotron frequency is significantly different to that of an inertial Alfvén wave [*Wahlund et al.*, 1998]. Consequently we restrict the frequencies to less than Ω_{O+} in the spacecraft frame.

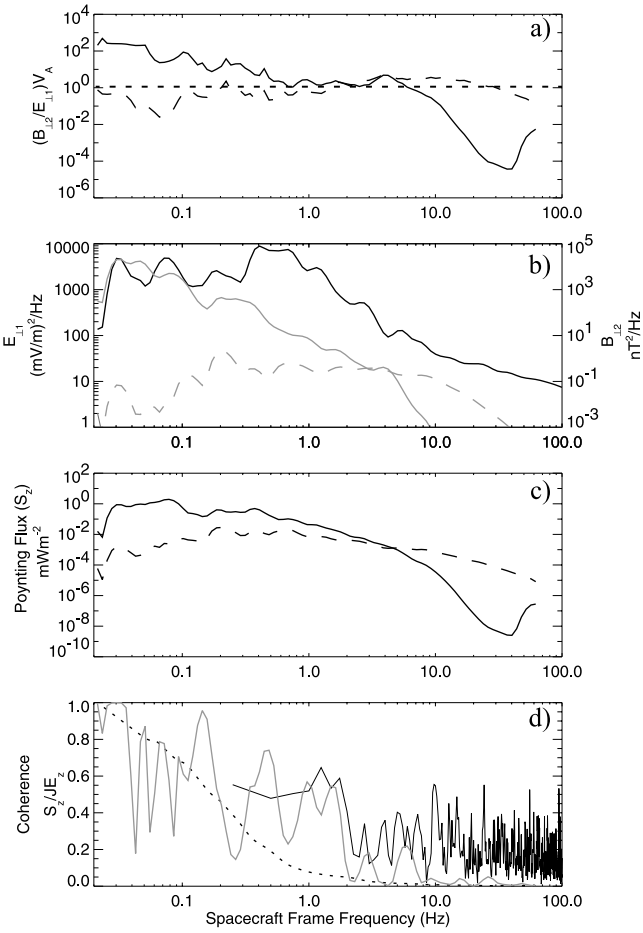

Figure 2. Case study spectral properties from wavelet transforms. Throughout dashed and solid lines show results obtained using the search coil and fluxgate magnetometers respectively. Panel a) shows $B_{\perp 2}/E_{\perp 1}$ multiplied by the local Alfvén speed ($V_A = 1.3 \times 10^7$ m/s). Panel b) shows the electric (black) and magnetic field (gray) spectra. Panel c) shows the field-aligned wave Poynting flux calculated in the frequency domain. Panel d) shows the coherence spectrum between the wave Poynting flux and the electron energy flux. The gray line represents the result obtained using the wavelet transform with the dotted line being the noise level, while the black solid line is the same result using the standard FFT technique.

[15] Below the 0.2 Hz lower limit of the range, the $B_{\perp 2}/E_{\perp 1}$ ratio, for reasonable values of ionospheric Pedersen conductivity, is more consistent with the operation of field-aligned currents. There may well be lower frequency Alfvén waves present at this time contributing to the rest frame wave spectrum at ultra low frequencies, however, for sufficiently small perpendicular scales these will appear through Doppler shift in the "Alfvénic" range defined above. The most important contribution in this range may be fieldline resonances [*Lotko et al.*, 1998; *Rankin et al.*, 1999]. Given that the FAST spacecraft travels at speeds between 5 and 7 kms^{-1} and such features can extend down

to kilometer scales perpendicular to B_o, these features will be represented in the spacecraft frame spectra almost purely at their Doppler shifted frequency, $k_\perp \cdot v_{spacecraft}$ (where $k_\perp$ is the wave number perpendicular to B_o). If such features satisfy the $E_{\perp 1}/B_{\perp 2}$ criteria defined above then they will be included in the database of these waves.

[16] We will now demonstrate from the case study data that it is over the "Alfvénic" frequency range from 0.2 Hz–20 Hz in the spacecraft frame that we observe the majority of the wave Poynting flux and show that variations in wave Poynting flux within this range are correlated with modulations in the field-aligned electron energy flux. Figure 2c shows the wave Poynting flux as a function of frequency based on the multiplication of wavelet transforms in $E_{\perp 1}$ (as shown in Figure 2b) and $B_{\perp 2}$ in frequency space making use of both the fluxgate (solid line) and search coil (dashed line) magnetometers. This curve is relatively flat over the "Alfvénic" range identified above but falls more steeply above 20 Hz and below 30 mHz (where one wave period represents the width of the entire interval). To compare the wave Poynting flux spectra with that found in the electrons we have taken data from fixed energy electron analyzers (ESAs) that sample the electron energy flux at ~2 ms. On FAST we have six such ESAs over the energy range from 74 to 2383 eV for the operating mode of the spacecraft at this time. The measurements of these are integrated to obtain a high-resolution version of the result shown in panel e) of Figure 1 albeit with somewhat lower fluxes due to the more limited energy range. If we now perform a cross-correlation between the wave Poynting flux and the electron energy flux derived in this way, the frequency range over which the waves modulate the particle fluxes can be directly identified. Figure 2d shows the results of this process using both wavelet (solid gray line) and FFT (solid black line) cross-spectral techniques. The dashed line is the spurious correlation expected from the wavelet technique for noise. Points above this can be interpreted to indicate some relationship between the two times series while values above 0.6 for the FFT result indicate correlated time series. From both techniques the signals become most clearly correlated at frequencies from ~0.1 Hz and up to 2 Hz. Above this range we see a sharp decrease in the wave coherence from both techniques. This shows that in the spacecraft frame the wave energy flux (or Poynting flux) and particle energy flux are most closely related (at least locally) over the frequency range from ~0.1 to 2 Hz which is in the center of the "Alfvénic" frequency range defined above.

3. Defining the Database

[17] Each wave event in the database has been First identified from a slope in the despun perpendicular magnetic field perturbation ($B_{\perp 2}$) equivalent to a current of 10 $\mu A/m^2$ or ~6 nT s^{-1} or greater. This current threshold eliminates large-scale Alfvén waves from the database. The upper frequency limit is effectively set by the recursive filter of the fluxgate magnetometer which, depending on the sampling frequency of the mode in operation at the time, limits the top end to ~22 Hz in the spacecraft frame. This frequency is above the oxygen cyclotron frequency (defined in section 2 as the upper limit of the frequency range where

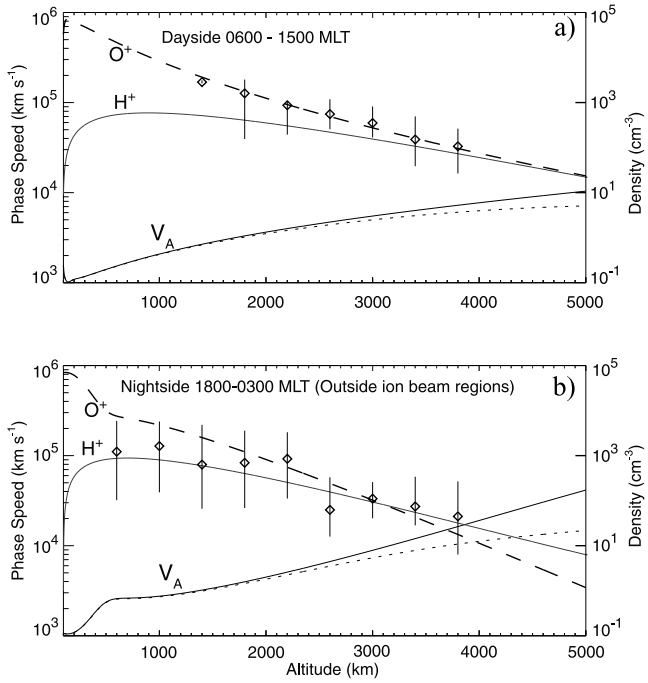

Figure 3. Density and composition models for the dayside (a) and nightside (b) auroral ionospheres. The dashed and gray lines here represent the density of O^+ and H^+ while the black line is the Alfvén speed, V_A, calculated from these and a dipole geomagnetic field model. The diamonds are median electron density values in 400 km width bins with the range of measurements in each bin represented by the error bars.

fluctuations are considered in this study as Alfvénic) at all altitudes above ~2000 km. This range could be extended through the use of search coil magnetometer measurements but this has not been performed at this stage. Over the interval where the slope of magnetic field ($B_{\perp 2}$) maintains the same sign, the change in the perpendicular electric field ($E_{\perp 1}$) in quadrature to the magnetic field change is determined and a value of $E_{\perp 1}/B_{\perp 2}$ calculated. If the value of this ratio is within an order of magnitude of the statistically determined value for V_A, shown in Figure 3, at the altitude of observation then the event is included in the database and the maximum electron energy flux and electron characteristic energy (defined as energy flux/flux) over that interval is recorded.

[18] The altitude dependency of V_A shown in Figure 3 has been determined from density and composition measurements for an H^+, O^+ and e^- in a charge neutral plasma using a variety of wave and particle techniques applied to several hundred orbits over the altitude range covered by FAST. The dotted line is the inertial Alfvén speed for the wave number $k_\perp = 2\pi/5000$ m. Densities are labeled O^+ and H^+ and measured on the secondary *y* axis. The diamonds represent the median electron density in altitude bins of 300 km width with the errors bars representing the full range of densities recorded in each altitude bin. The nightside profiles are fitted to the observed points ignoring the extreme low-density measurements found at times for altitudes above 3000 km. These low densities are measured

in ion beam regions as detailed by *Strangeway et al.* [1998], *Ergun et al.* [1998], and *McFadden et al.* [1999]. In such regions the Alfvén speed can be so high that identification of the Alfvén wave using the magnetic field perturbation becomes difficult and so we have not included them in this study. We also exclude those events where high time resolution, or burst electron data with full 2-D electron distributions at 80 ms is not available.

[19] The events included in the database number 3598 derived from a survey of orbits from the FAST mission with the first recorded event from October 1996 and the last from June 2000. Each event has been individually inspected by eye to ensure the quality of the statistics. There has been no bias in the selection of which orbits to examine based on MLT or other orbital parameters but rather the events included have been identified from a weekly examination of data recorded by the FAST satellite. Since the plots presented herein do not represent the results from a more rigorous automated survey of observations from FAST this study can only be considered as a preliminary indication of the characteristics of these waves and the coincident electron distributions. No doubt there are many more passes of the FAST spacecraft through the auroral oval containing Alfvén waves that have not been included in this study. We reserve the inclusion of these for a more complete statistical study.

4. Relationship to Optical Observations

[20] Under the spatial interpretation and for FAST spacecraft speeds, the frequency limits of the "Alfvénic" range identified here define a range of widths perpendicular to B_0 mapped to the ionosphere from ~10 km down to 100 m. These scales may be related to the widths of optical aurora and there have been a variety of optical forms identified in association with Alfvén waves over this range. *Trondsen et al.* [1997] observed multiple east-west aligned auroral arcs at widths of a few hundred meters consistent with expectations from acceleration in Alfvén waves. Observations reported by *Hallinan et al.* [2001] recorded in coincidence with observations from the AMICIST rocket have shown that these waves may be associated with rayed arcs or vortex streets on km scales aligned roughly east-west. *Lotko et al.* [1998] identified an arc of ~10 km width coincident with an Alfvén wave observed from FAST and characterized it as a field-line resonance.

[21] From spacecraft observations the form of the associated optical feature can partially be discerned from the wave polarization. It has been shown by *Volwerk et al.* [1996] that these wave fields go from largely linear to more circular polarization with increasing frequency in the spacecraft frame. At scales larger than 1 km these features were found to be largely linear while at smaller scales of the order of 200 m they appeared more circularly polarized. From a statistical study of FAST magnetometer data presented by *Stasiewicz et al.* [2000] and performed over the same frequency range as here and mentioned already in section 2.1, it was found that ellipticity in the Alfvén waves peaked at ~0.2 suggesting elongation of these features in the East-West direction. While a study of the polarization of the observed Alfvén waves is not included in this report, it can be said that $B_{\perp 2}$ (East-West) is mostly larger than $B_{\perp 1}$ (North-South). In the spatial approximation this is consistent with features elongated in the east-west direction.

[22] From the temporal perspective, given that the majority of events included in the database are on the poleward boundary of the oval it can be expected that most of these are more likely to be associated with dynamic impulsive optical features rather than slowly varying discrete auroral arcs. We however make no distinction here of the auroral morphology or duration associated with each event except to say that under the spatial assumption, the range of observed widths mapped to the ionosphere extending from 100 m up to ~10 km may be related to the narrow end of the arc widths identified by *Knudsen et al.* [2001] and to the narrowest of auroral features observed by *Trondsen et al.* [1997] and *Maggs and Davis* [1968].

5. Auroral Oval Distributions

[23] Figure 4a shows the distribution of Alfvén wave events observed over the auroral oval. Based on the definition of an event from above in section 3, Alfvén waves are observed throughout the oval but most commonly from 10 to 13 MLT. This region corresponds to the location of the polar cusps in which Alfvén waves are observed during nearly every traversal of this region by the FAST spacecraft. A second peak occurs from 21 to 01 MLT. The appearance of Alfvén wave events in this region is correlated with enhanced values of AE and from an inspection of Polar UVI data the strongest events observed occur during the expansive phase of magnetospheric substorms as detailed by *Tung et al.* [2001].

[24] Figure 4b shows the median value in each invariant latitude and MLT bin of the maximum or peak field-aligned wave energy flux for each event when mapped to 100 km altitude. This quantity has been calculated from half the maximum peak-peak variation in $E_{\perp 1}$ and $B_{\perp 2}$ for each event and labeled as $E_{\perp 1}$ and $B_{\perp 2}$ in Figure 4b and contains both upgoing and downgoing wave energy fluxes. From events where the full vector has been calculated however the Poynting flux is mainly pointed downward with some intervals of upwards Poynting flux consistent with the observations of *Volwerk et al.* [1996]. The wave energy density calculated in this way ignores the contribution from $E_{\perp 2}$ and $B_{\perp 1}$ since $E_{\perp 2}$ is not always measured. As a result the wave energy fluxes shown in Figure 2 provide an indication of the magnitude of the field-aligned wave Poynting flux rather than a measure of field-aligned Poynting flux vector. For an ideal MHD wave we could use $E \cdot B = 0$ to evaluate $E_{\perp 2}$ however since these waves carry a parallel to B_o electric field ($E_{\parallel}$) [*Chust et al.*, 1998] this is not strictly valid. The unmeasured contribution can however be expected to be smaller than the measured contribution to the field-aligned Poynting flux due to the expected wave polarization known from events when 3-D measurements are available [*Stasiewicz et al.*, 2000] (as already mentioned in section 4) and the FAST orbit which is largely transverse to the auroral oval. Consequently, it is generally true that $|E_{\perp 1}B_{\perp 2}| > |E_{\perp 2}B_{\perp 1}|$.

[25] Comparing the distribution of wave energy flux of Figure 4b with the event occurrence distribution of Figure 4a it is clear that while many wave events are observed in the dayside oval or cusp, the wave energy flux carried by these

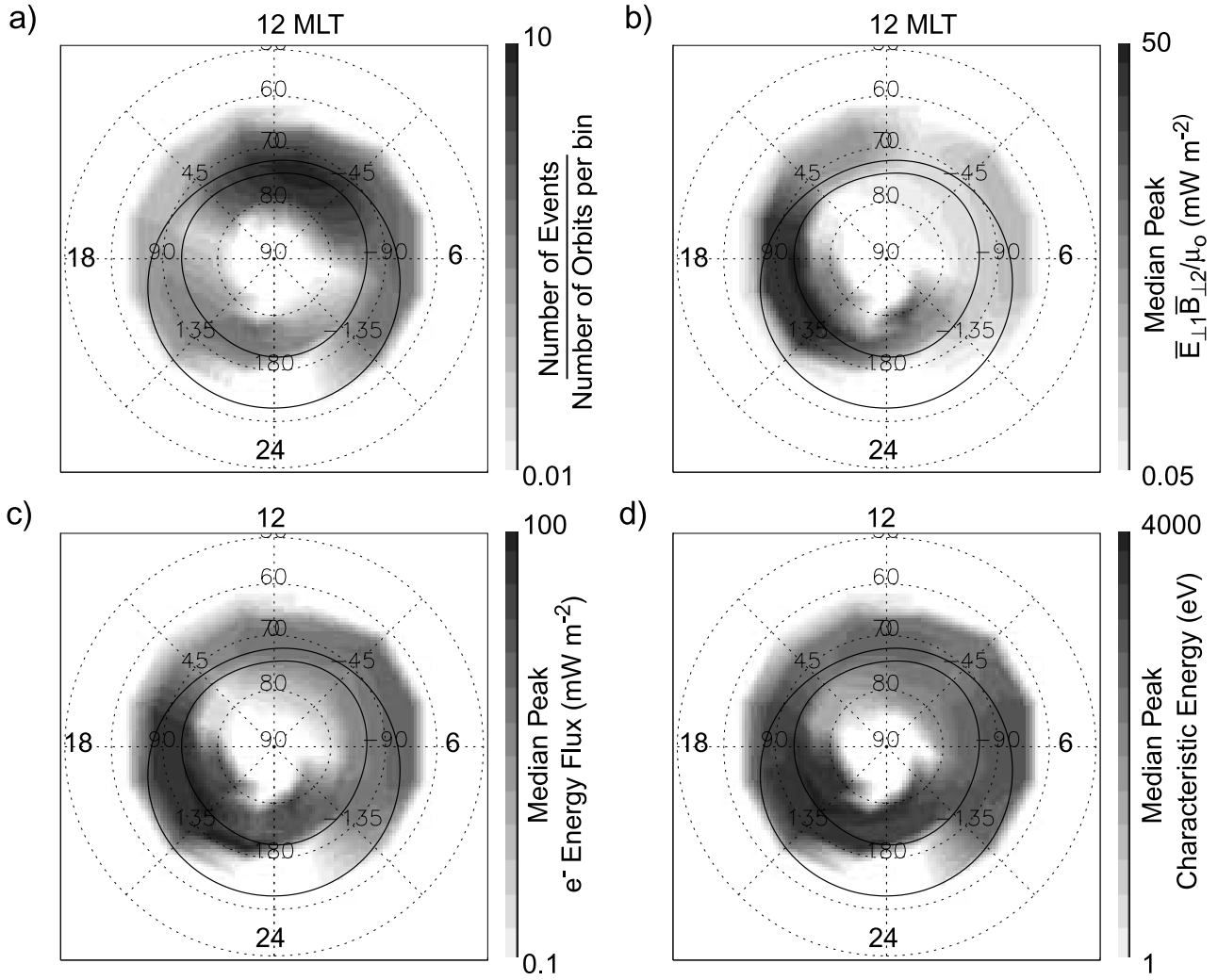

Figure 4. The distribution of wave event and coincident electron properties mapped to the ionosphere (at 100 km altitude) as functions of magnetic local time (MLT) and invariant latitude (ILAT). The solid concentric circles are the statistical location of the auroral oval. Panel a) shows the event distribution while the other panels show the median of the peak values found for each event for the quantities indicated in each MLT and ILAT bin.

waves is significantly less than for those observed in the premidnight sector. Whether this indicates that significantly more wave energy flux is reflected at altitudes above the spacecraft in the dayside oval or indicates differences in the wave source is unclear from the data alone and will be considered with the help of simulations in section 8.

[26] Figure 4c shows the median value of the maximum field-aligned electron energy flux mapped to 100 km altitude for each event in each MLT/ILAT bin. Care has been taken to exclude inverted-V and plasma sheet electrons from the calculations of these energy fluxes by eyeballing each event individually and setting an upper limit for the energy range used for the integration. Since the peak energy of the electrons accelerated by Alfvén waves in inverted-V regions is generally less than the energy of the monoenergetic peak and also less than temperature of the plasma sheet electrons, the results presented above provide a reliable measure of the electrons accelerated in the Alfvén wave. The distribution over the auroral oval is similar to that found for the wave energy flux. In the cusp region we find statistically that over the altitude range traversed by FAST the wave energy flux (Figure 4b) is roughly an order of magnitude less that the electron energy flux. In the premidnight and dusk sectors the electron and wave energy flux comparison still favors the electron energy flux however the difference is somewhat less. These observations suggest that if the waves are energizing the electrons then most of the acceleration has occurred above the spacecraft. This issue will be addressed more rigorously in sections 7 and 8 where we examine the altitude dependency of the wave and electron properties.

[27] Figure 4d shows the median value of the characteristic energy for each event in each MLT/ILAT bin. This indicates peak median energies premidnight up to 4 keV with peak median energies in the cusp region of the order of 100 eV.

[28] If we interpret the electron acceleration that occurs in these waves as a result of Landau resonance then the

maximum electron energy reached should be indicative of the maximum wave phase speed reached above the spacecraft. By using the density and composition model of Figure 3 this can then be used to indirectly estimate the altitude where much of the electron acceleration is occurring. Figure 4d shows that in the dayside oval we obtain median energies of ~100 eV thereby suggesting a peak Alfvén speed (or inertial Alfvén speed) at some altitude along the fieldlines mapping to the dayside oval of at least 6×10^3 km s^{-1}. The solid line in Figure 3a shows than that the minimum altitude from which electrons can be resonantly accelerated to this energy is ~3000 km. In the premidnight sector where the median characteristic energy is ~4000 eV the peak Alfvén wave phase speed is at least 3×10^4 km s^{-1}. To explain the most energetic electrons, which reach 10 keV (as seen in Figure 1) in this approximation, we require Alfvén speeds of up to 6×10^4 m/s. The solid line in Figure 3b suggests in this case that the minimum altitude at which this acceleration can occur is ~4500 km with the most energetic electrons arriving from heights well above 5000 km. A more subtle evaluation shows however, that in the absence of density cavities these source altitudes are an absolute minimum for acceleration to these energies since in addition to requiring the necessary wave phase speed the wave must also carry sufficient parallel field to accelerate the electrons up to the wave phase speed. Since the magnitude of this field decreases with increasing density it is very difficult, at least in the linear approximation, to accelerate electrons in this way below 4000 km or where significant ionospheric densities are present even if the wave phase speed is sufficient to account for the energy observed. Non-linear effects may be important in generating large parallel electric fields at lower altitudes [*Chust et al.*, 1998] however, it will become evident in the altitude-dependent wave and particle properties discussed in section 6 that in general the amount of acceleration occurring in the wave below FAST apogee (4175 km) is small relative to that which has occurred above the spacecraft.

6. Wave and Electron Energy Flux

[29] Figure 5a shows the dependency of electron energy flux on wave energy flux with the gray dots representing events with downgoing electron fluxes and the black crosses representing events with upgoing energy flux. The downward events far outnumber the upgoing events at FAST altitudes. Generally, it can be seen from this plot that increasing wave energy flux corresponds to increasing electron energy flux as may be expected if the wave accelerates the particles. The solid diagonal line corresponds to a slope of one or wave energy flux equal to electron energy flux. The electron energy flux generally lies above this line showing that at FAST altitudes the electron energy flux exceeds the wave energy flux. This was essentially demonstrated by the polar plots of Figures 4b and 4c. The significant new insights gained from Figure 5a are however, that the upward electron energy fluxes more closely follow changes in wave energy flux and that the energy fluxes of the upgoing events are generally less than for the downgoing case with values more comparable to the wave energy flux.

[30] These results are consistent with a model where the most of the wave acceleration of the electrons occurs above the spacecraft. The downgoing fluxes have absorbed a significant fraction of the incoming wave energy flux by the time they reach FAST altitudes and so are observed in energy fluxes exceeding the wave energy flux. Since much of the wave energy accelerating the particles has already been absorbed, the downgoing fluxes will generally be not as well correlated as the upgoing fluxes with variations in the magnitude of the wave Poynting flux observed at FAST. Some of the remaining observed downgoing wave energy flux is reflected at altitudes below FAST and the upgoing wave then accelerates electrons back up the fieldline as it propagates out into the magnetosphere. It can be expected that these upgoing electrons will be significantly less energetic due to the depleted energy flux in reflected the wave and the effects of the ionospheric density on the parallel electric field of the inertial wave at FAST altitudes [*Chaston et al.*, 2003a]. With a few exceptions this is observed to be the case. Figure 5b shows the characteristic energy of the upgoing electrons is less than 100 eV. Figure 5c shows that while the flux in both upgoing and downgoing electrons is strongly dependent on the wave energy flux the upgoing fluxes are generally less those downgoing. The energy of these upgoing electrons also is indicative of the additional energy gain in the wave possible for the downgoing electrons below the altitude at which they are observed. This shows that while electron acceleration in Alfvén waves does occur below FAST altitudes it yields energies and fluxes of the order of 10% of that reached in the wave acceleration process occurring above the satellite.

7. Altitude-Dependent Properties

[31] The dispersion and dissipation of Alfvén waves above the auroral oval is strongly altitude dependent. The altitude dependency of macroscopic features such as the magnetic field, density and composition are essential ingredients in modeling the microscopic processes that lead to electron acceleration in these waves. We shall now discuss how these macroscopic features manifest themselves in wave and particle observations by first determining the average perpendicular width of the events observed, and under the assumption that the observed structure is largely spatial, use this width as a proxy for the perpendicular wavelength of the wave ($\lambda_\perp$). This "wavelength" is then used in a simulation model for determining the expected variation in wave amplitudes and Poynting flux as a functions of altitude due to wave reflection for direct comparison with the averaged wave and particle results observed from FAST.

7.1. Width of Alfvénic Features

[32] Figure 6 presents the variation in the perpendicular width of the observed events in the fluxgate magnetometer results. These have been scaled with the magnetic field to provide a measure of their width in the ionosphere at 100 km. The result shows that the median width of these features map to ~1000 m at the ionosphere. The minimum width resolvable at spacecraft altitudes from the fluxgate magnetometer is limited to ~100–200 m due to the recursive filter on this instrument. The range observed at each altitude is represented by the error bars which extend from widths in the ionosphere of 100 m to greater than 10 km or in the

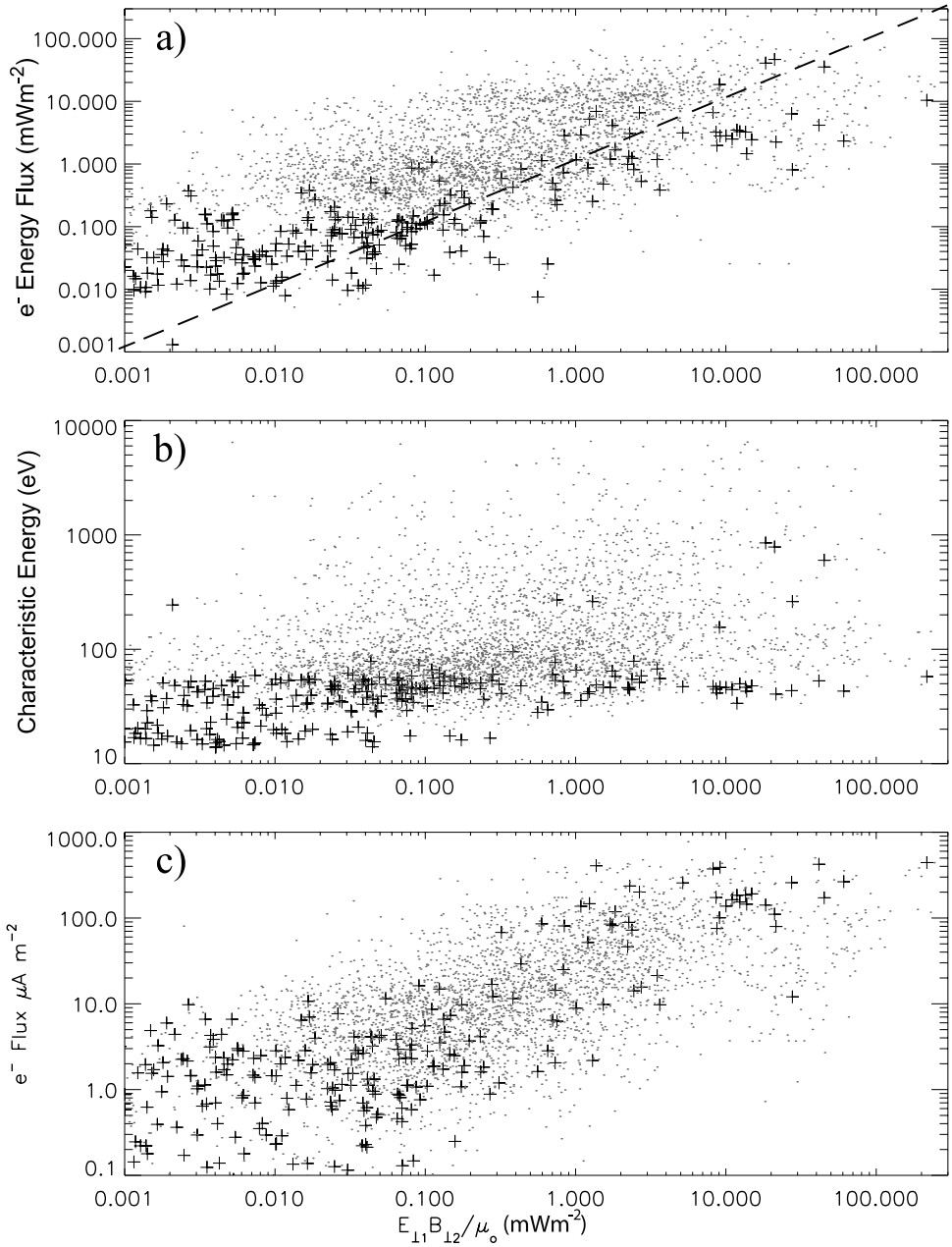

Figure 5. Electron properties as a function of wave energy flux mapped to the ionosphere (at 100 km altitude). Gray points indicate events with downgoing electrons while black crosses show events with upgoing electrons. Panel a) shows the variation in electron energy flux (at 100 km altitude), b) shows variation of characteristic energy and c) shows the variation in electron flux or current (at 100 km altitude).

spacecraft frame over a frequency range from ~0.2 Hz–20 Hz. Smaller scale structures may exist which the fluxgate magnetometer does not resolve however since the median value falls in roughly the center of the observed range at each altitude (shown by the error bars) these smaller scale events are in the minority. In the purely spatial interpretation, which *Stasiewicz et al.* [2000] has shown is perhaps appropriate at these small scales, these widths correspond to that distance along the spacecraft trajectory where the sign of the wave magnetic field gradient remains the same. As an approximation, we can then think of each width as 1/2 the perpendicular wavelength ($\lambda_\perp$) of the wave in the ionosphere. Motivated by this result a perpendicular wavelength in the ionosphere of 2 km will be used in the simulations employed in the remainder of this report.

7.2. 1-D Inertial Alfvén Wave Simulation

[33] We implement a 1-D simulation code based on the model equations from *Thompson and Lysak* [1996] for a plasma defined by the statistical density and composition curves shown in Figure 3 but extended to 30,000 km altitude [*Chaston et al.*, 2003b] with a dipole magnetic field. It is assumed in this model that the wave is spatially periodic and invariant in the North-South and East-West

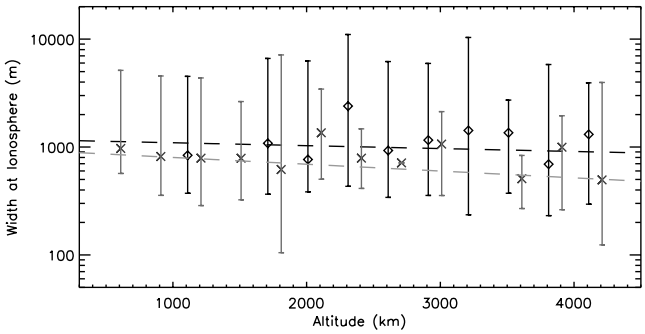

Figure 6. Widths of Alfvénic current filaments mapped to the ionosphere (at 100 km altitude). Gray and black correspond to dayside and nightside events respectively. The diamonds and crosses show the median value in altitude bins of 300 km width in altitude. The size of the bars indicate the range of widths observed at that altitude. The dashed lines are linear fits to the data.

directions respectively. Since the formalism is described in the aforementioned publication we do not repeat the model equations here. The wave is launched from the magnetospheric end at 30,000 km using an applied potential of 600 V distributed as a Gaussian with a half width of 1s. For the reasons indicated above in section 6.1, the perpendicular wavelength of the wave in the ionosphere is assumed to be $\lambda_\perp$ = 2 km which scales in altitude with square root of the geomagnetic field strength. These model parameters provide a maximum wave amplitude for the nightside profile of 1 V/m and 0.6 V/m in the dayside case. The field-aligned electron acceleration that occurs in the simulation is purely due to the electron inertial effect which in the local approximation provides a parallel electric field given by $E_\parallel/E_{\perp 1} = (k_\parallel k_\perp \lambda_e^2)/(1 + k_\perp^2 \lambda_e^2)$ with $E_{\perp 1}/B_{\perp 2} = V_A(1 + k_\perp^2 \lambda_e^2)^{1/2}$ where λ_e is the electron skin-depth defined as c/ω_{pe} with ω_{pe} being the electron plasma frequency.

[34] Since the $E_\parallel$ carried by the wave is periodic with $\lambda_\perp$ in the transverse direction, the model describes an array of arcs of infinite east-west extent separated by the perpendicular wavelength of the waves (mapped to the ionosphere) and moving north or south at the perpendicular phase speed of the wave in the ionosphere. This pattern is similar to the observed arcs described [*Trondsen et al.*, 1997]. As we have driven the simulation with a Gaussian pulse in the potential, this pattern appears then fades once the wave has reflected from the ionosphere. However, the simulation could equally be driven by a continuous oscillation at the magnetospheric boundary to create auroral arcs lasting as long as the oscillating potential persists in the magnetosphere. Because of this flexibility the simulation is equally applicable to impulsive/burst events and longer duration features. For 3-D structures such as the vortices observed by *Hallinan et al.* [1999] it is unclear how the electron acceleration process will be modified, however the magnitude of the electric field will still be determined by the ratio of the perpendicular scale of the wave to the electron inertial length as modeled here.

[35] The single wave frequency and perpendicular wavelength used, as defined above, fall in the middle of the observed frequency range and associated spatial scales identified in sections 2, 3, and 4 of the statistical study. Changes in wave frequency and wave number from these values over the ranges identified do not appreciably alter the comparison with observations discussed below except at very small scales and high frequencies. It has been demonstrated by *Chaston et al.* [2003b] that waves over the entire range are capable of accelerating electrons to form aurora.

[36] Since this is a 1-D model it is assumed that gradients in density perpendicular to the geomagnetic field are on larger scales than the perpendicular wavelength of the wave. This assumption at times may not be appropriate however the ability of this simulation to reproduce in detail the electron distributions observed in Alfvén waves and the time dependent energy spectra associated with intervals of Alfvénic activity observed from FAST has been shown previously by *Chaston et al.* [2003a].

7.3. Observed Altitude-Dependent Wave and Particle Properties

[37] Figures 7a and 7b show the variation of the wave electric ($E_{\perp 1}$) and magnetic ($B_{\perp 2}$) fields with altitude. The black diamonds represent the peak-to-peak amplitude of events observed in the nightside oval in bins of width 300 km in altitude. The error bars show one standard deviation in each bin and have been drawn in one direction only as we are plotting on a logarithmic scale. The gray crosses and error bars represent the same for the dayside oval but have been offset by 100 km from the nightside points for clarity. The gray and black dashed lines are linear fits to the observations intended to show the general trend with altitude. The black and gray solid lines shown in Figures 7a and 7b correspond to the amplitudes of the wave fields for the simulated downgoing Alfvén wave propagating through the nightside and dayside density and composition profile shown in Figure 3 respectively and before reflection from the ionosphere. In calculating the simulated electric field and magnetic fields no corrections have been made to account for losses in wave energy except via reflection. These results have been scaled to pass through the highest altitude portion of the trend lines in each case to model the expected variation in the observed field quantities with altitude due to the changes in V_A and downgoing wave energy losses through wave reflection.

[38] The trend lines show that the observed electric field for both the dayside and nightside events decrease with decreasing altitude. This is expected with the decreasing Alfvén speed over this altitude range. However, comparing the observed change with the simulation result shows that the observed field decreases over the FAST altitude range by roughly 5 times the amount of the simulated fields. In the observed magnetic field there is a small increase with increasing altitude, however again the observed amplitude at lower altitudes is significantly less than the simulated result. Despite these changes, Figures 7c and 7d show that the observed $E_{\perp 1}/B_{\perp 2}$ ratio remains Alfvénic over the altitude range studied. Changing the model perpendicular wave number at the ionosphere from the $2\pi/2$ km value used here does not appreciably effect the simulated variation in $E_{\perp 1}$ and $B_{\perp 2}$ with altitude over the FAST range except for very large values where the inertial effect strongly modifies wave dispersion. The observed diminishing wave amplitudes observed relative to those simulated suggests

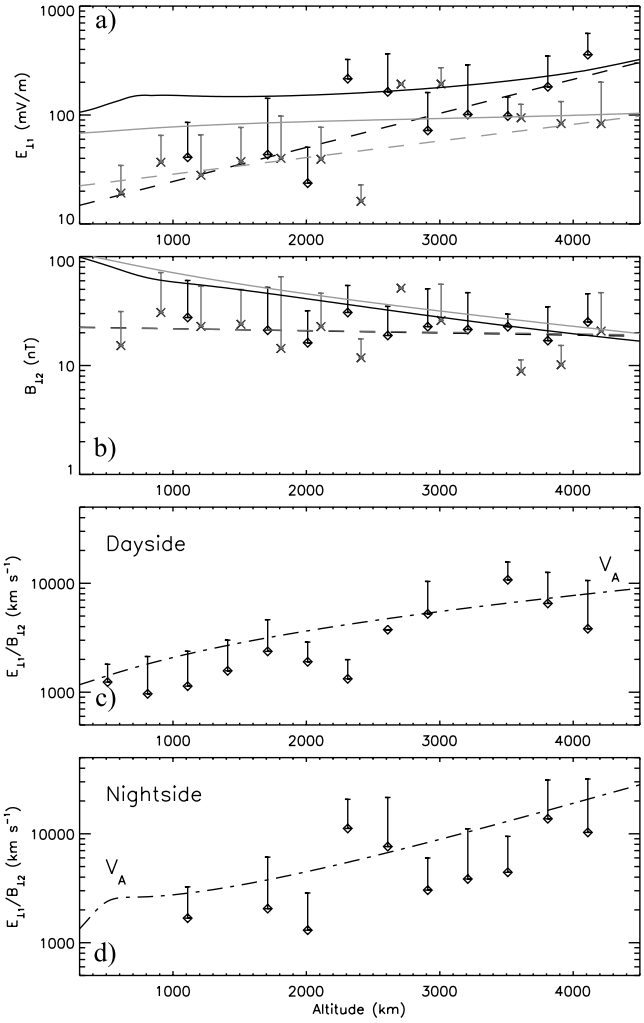

Figure 7. Altitude-dependent fields quantities. Gray and black correspond to dayside and nightside events respectively. Panels a) and b) show the variation in the wave field amplitudes with altitude. Each point (diamonds—nightside, crosses—dayside) is the median value in an altitude bin spanning 300 km in altitude. The error bars are the standard deviation in each bin and are drawn only in one direction due to the logarithmic scale. The solid lines correspond to the simulation result for each quantity while the dashed lines are linear trendlines. Panels c) and d) show the $E_{\perp 1}/B_{\perp 2}$ ratios for the dayside and nightside events respectively as function of altitude with the dot-dashed line being the Alfvén speed based on the result of Figure 3.

that as the wave travels down the fieldline toward the ionosphere over the FAST altitude range, wave energy is lost in addition to that lost through partial reflection on the Alfvén speed gradient. This is consistent with particle energization and Alfvén wave damping over the FAST altitude range.

[39] Figure 8a shows the observed decrease in wave energy flux with altitude. The energy fluxes shown here are mapped to an altitude of 100 km and the crosses and diamonds represent-dayside and nightside events in 300 km width altitude bins as previously in Figure 7. The error bars on each point are again one standard deviation and have been plotted in only one direction since we are plotting on a logarithmic scale. The black and gray dashed and solid lines are the linear trend lines from the observations and the result from the simulation before wave reflection from the ionosphere. The simulation results have been scaled to coincide with the trendlines at 4600 km. It can be seen that both nightside and dayside fluxes (observed and simulated) generally decrease with decreasing altitude over the FAST altitude range. The simulation result shows that reflection can account for a 10% decrease in the dayside incident wave Poynting flux and about 50% in the nightside case over the FAST altitude range for the statistical density and composition profiles used. The observed changes in wave energy

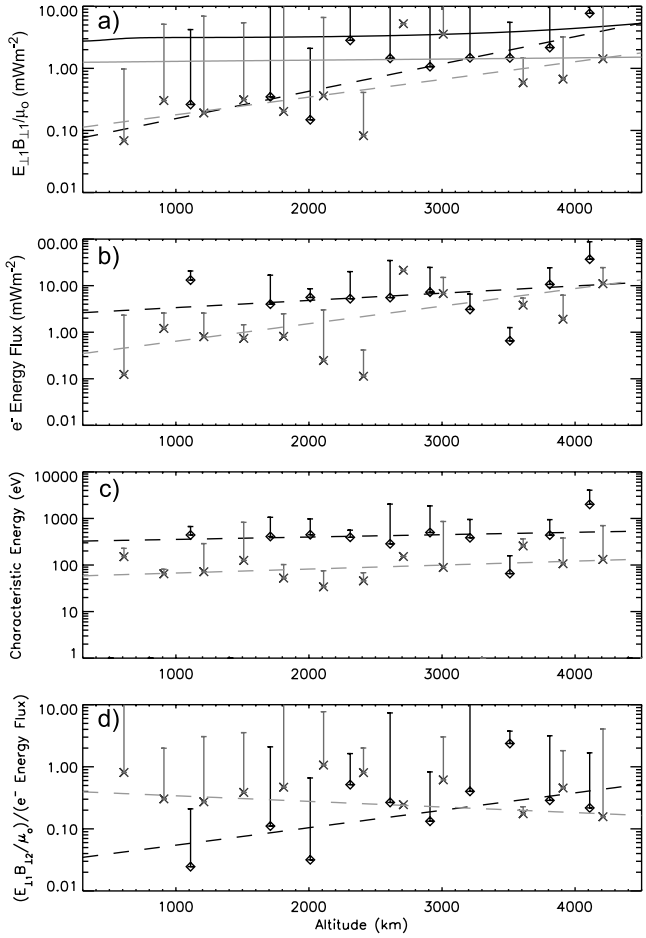

Figure 8. Altitude-dependent wave energy and electron properties. Gray and black correspond to dayside and nightside events respectively. Dashed lines are linear fits to the data while solid lines show the result from the simulation described in the text. Each point is the median value in a bin of 300 km width in altitude. The error bars are the standard deviation in each bin and are drawn only in one direction due to the logarithmic scale. Panel a) shows the variation in wave energy flux mapped to the ionosphere (at 100 km altitude) with altitude. Panel b) shows the variation in electron energy flux mapped to the ionosphere (at 100 km altitude) with altitude. Panel c) shows the variation in the characteristic energy (energy flux/flux) of the electrons with altitude. Panel d) shows the variation in the ratio of wave energy flux to electron energy flux with altitude.

flux over this altitude range are however more than an order of magnitude. This result has two possible explanations: first much of the wave energy flux incident from above at FAST apogee (4175 km) is absorbed by the plasma before it reaches the ionosphere or second the phasing of the electric and magnetic fields is such that the field-aligned Poynting flux (or wave energy flux) is small at these altitudes. The second possibility is expected if the ionospheric Alfvén resonator (IAR) [*Lysak*, 1991] is operating. This provides a standing wave between the ionosphere and the gradients in Alfvén speed above it for which the wave Poynting flux may approach zero. The effects of this resonance did not appear in the simulation results plotted in Figures 7 and 8 since we considered the wave before interaction with the ionosphere. We reserve discussion of the contribution of the IAR until section 8.

[40] If we now consider wave energy absorption by the plasma, the obvious recipients for lost wave energy are the field-aligned electrons observed coincident with the wave energy flux. With this in mind Figures 8b and 8c show the variation in electron energy flux and electron energy mapped to the ionosphere at 100 km altitude as functions of the altitude of observation. Given that the wave energy flux shown in Figure 8a is almost an order of magnitude less than the electron energy flux (Figure 8b) over the altitude range examined and that the standard deviation in these electron energy fluxes is also significantly larger than the magnitude of the wave energy flux, it is not possible to statistically verify if the observed decrease in wave energy flux with decreasing altitude is correlated with an increase in electron energy flux. Since (from Figure 5) it is known that the upgoing wave energy flux is of similar magnitude to the electron energy flux a more meaningful comparison would be to compare the energy fluxes of the upgoing electron events with the correlated upgoing wave energy fluxes. Unfortunately we have insufficient altitude coverage in these events to perform this comparison.

[41] It is also possible, given the limited number of events included in the database that the events at lower altitudes are of lower wave energy flux for reasons other than altitude dependency. To eliminate this possibility Figure 8d shows the value of the wave energy flux normalized by the electron energy flux. For the nightside events we obtain a decrease in this ratio with altitude consistent with the dissipation of wave energy through electron energization. For the dayside events the ratio actually increases with decreasing altitude. From, Figures 8b and 8c however it is clear that since there is no significant increase in electron energy flux or energy over the FAST altitude range, then the energy gain for electrons from waves over the range of altitudes covered by the FAST satellite is small relative to that which occurs above FAST's apogee at 4175 km.

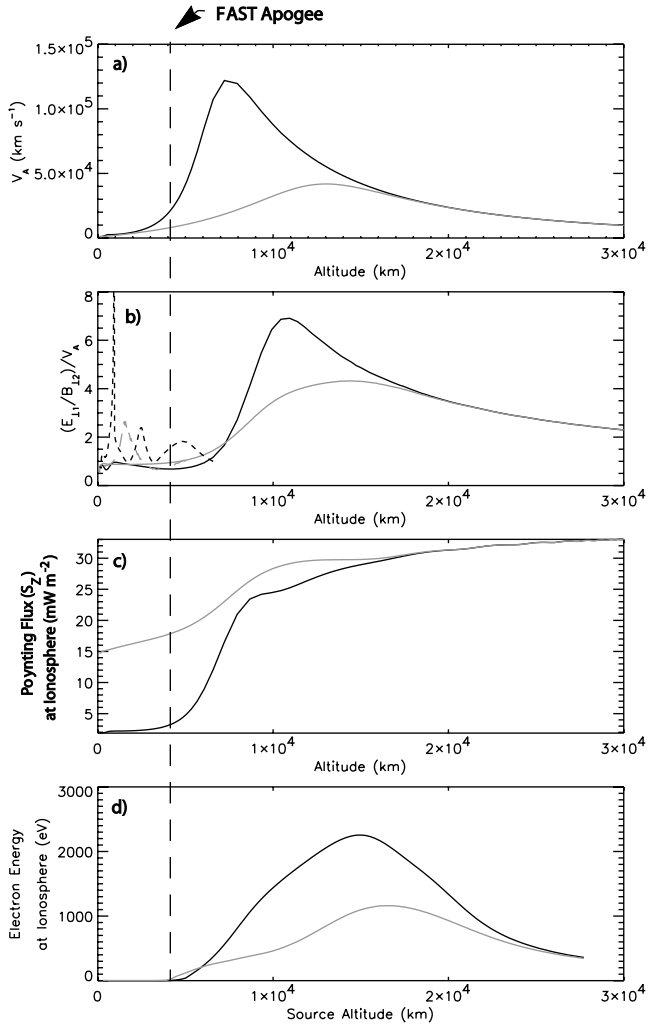

Figure 9. Simulation results as functions of altitude. Gray and black correspond to dayside and nightside events respectively. Panel a) shows the variation in the Alfvén speed. Panel b) shows the $E_{\perp 1}/B_{\perp 2}$ ratio for the downgoing wave normalized in terms of the Alfvén speed at each altitude. The dot-dashed lines here show variations in this ratio over the altitude range of the ionospheric Alfvén resonator discussed in the text. Panel c) shows the field-aligned wave Poynting flux mapped to the ionosphere (at 100 km altitude) for the downgoing wave. Panel d) shows the energy at the ionosphere (at 100 km altitude) reached by thermal electrons originating from different source altitudes after being accelerated in the wave field.

8. Discussion

8.1. Electron Acceleration

[42] We now discuss how the statistical wave and particle observations may be interpreted as the result of inertial Alfvén wave propagation, the operation of the ionospheric Alfvén resonator, and electron acceleration in the parallel electric field of the inertial Alfvén wave. With this intention Figure 9 shows the results from the simulation described in section 6.2. The fine gray and thick black lines correspond to dayside and nightside quantities respectively. Panel a shows the Alfvén speed as a function of altitude over the simulation range. Large gradients in the Alfvén speed occur both above and below the peak in these speeds particularly in the night side case at 7000 km and for the dayside case around 13,000 km. Alfvén waves incident on the ionosphere and these gradients experience reflection leading to the formation of a resonant cavity for Alfvén waves between the ionosphere and the Alfvén speed gradient above to form the IAR referred to already in section 6.3. The expected

$E_{\perp 1}/B_{\perp 2}$ ratio as a function of altitude from the simulation is shown in Figure 9b. The solid lines shown in this panel represent the wave as it travels down the geomagnetic field before interaction with the ionosphere while the dashed lines show this ratio after this time. The spiky character of the dashed lines at low altitudes is associated with the operation of the IAR with each spike corresponding to an anti-node of the resonator in $E_{\perp 1}$.

[43] We now use the simulation results shown in Figure 9 to explain the major observational results of this report:

1. It was shown in Figure 4 how the wave energy fluxes above the nightside oval are significantly larger than above the dayside oval. It was suggested that this was due to differences in the wave source.

Figure 9c shows the simulated downgoing field-aligned wave Poynting flux mapped to the ionosphere at 100 km altitude as a function of altitude with the thick black and fine gray lines corresponding to wave propagation in the nightside and dayside density profiles of Figure 3 respectively. The decreasing magnitude of the downgoing field-aligned Poynting flux shown here in both the dayside and nightside case is purely due to wave reflection since wave damping is not included in the simulation. The steeper Alfvén speed gradient above 4000 km for the nightside profile results in stronger wave reflection above FAST altitudes and only 10% of the wave Poynting incident flux from 30,000 km penetrates below FAST apogee. It is possible within the density range identified in Figure 3 for steeper density gradients in V_A to exist thereby providing more complete reflection and the possibility of observing accelerated electrons at FAST altitudes with no evidence of an Alfvén wave. For the dayside case the greater ionospheric scale height provides more gentle gradients in V_A and we find 50% of the incident wave Poynting flux from 30,000 km penetrates to FAST altitudes and to the ionosphere below. This results in significantly greater Poynting fluxes in the dayside case at FAST altitudes relative to the nightside case for the same applied potential at the magnetospheric end. The fact that Figure 4b indicates that the observed wave energy fluxes in the cusp (dayside) is in fact much less than for the polar cap boundary (nightside) suggests that the source for the Alfvén waves observed above the dayside oval may be significantly less energetic than that associated with the nightside events.

2. Figures 4b and 4c showed that the largest electron energy fluxes and characteristic energies are observed premidnight on the polar cap boundary.

To determine if this can be accounted for from simulations, Figure 9d compares the final energy of an electron when it is lost to the atmosphere as a function of source altitude (i.e. the altitude at which it becomes resonant with the wave) for the nightside (or polar cap boundary) and dayside (or cusp) cases. From this figure it can be seen that consistent with observations the night side case provides peak electron energies twice as large as the dayside result even though the wave Poynting flux for the dayside case at FAST altitudes is more than 5 times larger. In reality, the observed energy difference can be expected to be significantly greater than a factor of 2 because the observed wave energy fluxes in the dayside oval are typically much less than found in nightside events (as shown in Figure 4b).

3. Figures 8b and 8c suggest that limited electron acceleration in Alfvén waves occurs at FAST altitudes (<4175 km) with most of the energy gain occurring above FAST apogee.

In agreement with observations the simulation results shown in Figure 9d, indicate that, for the statistical density and composition profiles, the acceleration process is over before the wave reaches FAST apogee at 4175 km. The greatest rate of energy gain occurs where the wave encounters the peak in the Alfvén speed from above to yield the fastest phase speeds and the largest parallel wave fields. This occurs as the wave partially reflects on the strong gradients in V_A which further enhances the parallel wave field over the altitude range from 1 to 2 R_E for the nightside case and at higher altitudes for the dayside case [*Chaston et al.*, 2002]. This explains the result shown in Figure 9d which indicates that the most energetic electrons accelerated by the wave arrive at the ionosphere from a source altitude of ~15,000 km.

It should be remembered however, that the energy/altitude dependence shown in Figure 9d represents a median result from a large range of possible density/composition profiles as indicated by the large error bars of Figure 3. The most obvious exceptions to the result shown in Figure 9d are those events where upstreaming field-aligned electrons are observed at FAST. Such events are usually found in regions of lower densities than the statistical medians used here and sometimes within cavities. Lowering the density specifically for these cases as performed by *Chaston et al.* [2003a] can allow upwards and downward acceleration at FAST altitudes in the simulated Alfvén waves to energies of a few hundred eV.

A more detailed analysis of the consistency between observations and simulations based on a case study event [*Chaston et al.*, 2002] suggests that the observed wave is capable of accelerating electrons at lower altitudes than possible from the simulated linear inertial wave and of providing energies somewhat greater than achievable from the simulation for realistic wave amplitudes. Nonetheless, the picture for electron acceleration in Alfvén waves obtained through the statistical results shown here is largely consistent with that obtained from simulating electron acceleration in the parallel to B_o electric field of an inertial Alfvén waves where most of the electron acceleration occurs above 4175 km.

4. In Figure 8a it was shown that the wave energy flux decreases by more than an order of magnitude over the FAST altitude range.

[44] Given that the wave energy fluxes that are observed at FAST apogee are an order of magnitude less than the electron energy fluxes it is still likely that this energy is lost through electron acceleration even though no discernible increase in electron energy flux is observed over this range. In fact, it was shown in Figure 5b that the electron energy fluxes and wave energy fluxes for the upgoing events are well correlated and of similar magnitude suggesting the dissipation of wave energy via Landau damping [*Lysak and Lotko*, 1996] and electron acceleration as modeled here over this altitude range.

[45] An alternative explanation to account for the observed decrease in wave energy flux, as mentioned in section 7, is the operation of the IAR. For a perfectly resonant wave the

phase difference between $E_{\perp 1}$ and $B_{\perp 2}$ is 90° or 270° thereby providing zero Poynting flux. For the purely propagating wave, which will be provide the greatest Poynting flux, these fields are 0° or 180° out of phase. Since neither the ionosphere or the Alfvén speed gradient are perfect reflectors or transmitters the actual phase difference in the IAR can be expected to be intermediate between these values [*Lysak*, 1991] thereby providing an intermediate value for field-aligned Poynting flux over the altitude range of the resonator. From the peaks and troughs in the dot dashed lines of Figure 9b it can be seen that this phase difference is not constant over the altitudinal extent of the resonator, which includes the FAST altitude range. This allows for significant changes in the magnitude of the field-aligned Poynting flux with altitude, as observed, and without the need for dissipation.

[46] However, using a more complete ionospheric model *Lessard and Knudsen* [2001] indicate that for typical nightside ionospheric profiles there is minimal reflection from the ionosphere for wavelengths in the ionosphere less than 2 km and frequencies greater than 0.4 Hz. This precludes the operation of the IAR for small-scale Alfvén waves and suggests an ionospheric source for upgoing small-scale Alfvén waves. Despite this result the IAR has been identified in Freja and FAST data for km scale Alfvén waves [*Grzesiak*, 2000; *Chaston et al.*, 2002] suggesting that at least for these widths the resonator can function. What makes the resonator an unlikely candidate to account for altitude dependency of the wave energy flux is the decrease in the amplitude of $E_{\perp 1}$ with altitude beyond that expected due to changes decreasing V_A and reflection as shown in Figure 7a. While this suggests that the IAR is not a sufficient explanation for the altitude dependency of the wave energy flux, it does not preclude the operation of the ionospheric resonator accounting for some of the observed variation.

[47] Other processes to account for the observed decrease in wave energy flux over the FAST range include ion heating and mode conversion to electrostatic waves. Ion heating is unlikely to account for the total decrease since ion energy fluxes and energy densities are typically an order of magnitude or less than the observed wave energy flux and energy density. Mode conversion to slow ion acoustic [*Seyler et al.*, 1998] and electron acoustic waves [*Berthomier et al.*, 1999] or to smaller scale inertial waves [*Stasiewicz et al.*, 2000] (which are virtually electrostatic) have been suggested to account for the high frequency spectrum observed in association with these waves at low altitudes. However, because of the form of the observed spectra the amount of electromagnetic wave energy lost to these waves is small unless they are being continually dissipated. *Seyler* [1990] has shown theoretically that the evolved spectra for inertial Alfvén waves follow a $k^{-5/3}$ law. The observed spectra shown in Figure 2b indicate that the wave power in the electric field at frequencies greater than 1 Hz follows an $f^{-(1.5-2)}$ law. If we interpret these frequencies as largely the result of Doppler shift then the observed spectra agrees well with Seyler's simulations for inertial Alfvén waves. In this case the wave power at higher frequencies in the spacecraft frame or smaller scales is much less than at the spacecraft frame frequencies where $E_{\perp 1}/B_{\perp 2} \sim V_A$. And so the electrostatic modes cannot be the final depository of wave energy flux losses over the FAST altitude range.

8.2. Source Mechanisms

[48] From the above discussion it seems almost certain that the sources of Alfvénic wave activity observed from FAST are not local but rather are magnetospheric. *Wygant et al.* [2000, 2002] provides evidence for a magnetospheric source for the Alfvénic fluctuations seen from FAST showing observations of Alfvén waves and field-aligned electron acceleration at 4–6 R_E altitude from the Polar spacecraft. These waves occur on a variety of scales not dissimilar from the observations from FAST and map along fieldlines to the polar cap boundary near midnight were the most intense events from FAST are observed.

[49] There are many ways for shear Alfvén waves to be generated within the magnetosphere, however some may be more likely candidates based on where these waves are observed. It became apparent in section 4 that these waves are most commonly seen from FAST in the cusps and polar cap boundary near midnight. These regions are on the boundary between open and closed fieldlines close to noon and midnight perhaps suggesting an association between magnetic reconnection at the subsolar point or from a nightside neutral line during substorm expansion. In fact, *Keiling et al.* [2001] has shown the association between similar waves observed from the Polar spacecraft at higher altitudes and substorm onset and expansion phases. A possible scenario for the generation of these waves through the reconnection process may begin with the unfolding of fieldlines from the reconnection separatrix which is in essence a compressional Alfvén wave. It has been shown how these waves may then mode convert into shear Alfvén waves on Alfvén speed gradients perpendicular to B_o [*Hasegawa and Chen*, 1975] that are known to occur in the plasma sheet boundary layer [*Goertz and Smith*, 1989]. Simulations have been performed by *Allan and Wright* [2000] which show the efficacy of this process for producing shear Alfvén waves in the plasma sheet boundary which travel Earthward toward the polar cap boundary where they may be observed by FAST.

[50] An appealing feature of this model is in its ability to continuously pump Alfvén wave energy into the plasma sheet boundary layer from the reconnection site or source of the compressional wave and along the waveguide toward the Earth. Through phase mixing this may allow wave energy to continually be supplied to dissipative scales close to λ_e (in the inertial case) or ρ_a (the ion acoustic gyro radius for the kinetic case) to account for the electron acceleration observed along large sections of plasma sheet boundary layer fieldlines and into the poleward edge of the auroral oval as suggested by observations from Polar and FAST. The smallest perpendicular scales produced in the simulations of *Allan and Wright* [2000] when mapped to the ionosphere amount to ~50 km so it remains to be demonstrated whether phase mixing of these large scale shear waves can provide waves at strongly inertial and kinetic scales such as those observed at FAST. Other mechanisms by which smaller scales may be produced in Alfvén waves have been reviewed by *Wygant et al.* [2002] in the light of Polar observations.

[51] Recent kinetic simulations of the reconnection process suggest that it may be possible to generate waves at

kinetic and electron inertial scales directly from the diffusion region. These simulations have emphasized the importance of nonideal MHD terms in the generalized Ohm's law including the Hall term and those associated with electron inertia and electron pressure [*Shay et al.*, 2001]. Electrons in the diffusion region decouple from the magnetic field to form a current layer with width of the order of λ_e thereby providing an obvious source of inertial Alfvén waves [*Gekelman et al.*, 1997]. When a significant component of the magnetic field perpendicular to the plane of the X-line is included, the ions decouple from the magnetic field to provide ion current layers with width of the order of ρ_a thereby providing a source for kinetic Alfvén waves. In both cases strong turbulence develops which may account for the large Poynting fluxes and disordered waveforms seen from Polar and FAST.

[52] Other means for the generation of Alfvén waves along these fieldlines include the instability to Alfvén waves of the ion and electron beams that populate the plasma sheet boundary layer. *Angelopoulos et al.* [2003] from observations from the Polar and Geotail spacecraft argues that reconnection flows are unstable to Alfvén waves and can experience "braking" due to the emission of Alfvén waves to account for lack of observations of near-Earth reconnection flows and provide wave Poynting flux into the auroral oval. Plasma instabilities such as the current driven kink instability [*Gary*, 1976] and ion beam driven magnetosonic and ion cyclotron waves associated with anisotropic ion flows at speeds of the order of the local Alfvén speed have been demonstrated [*Chaston et al.*, 2000] to grow to levels sufficient to account for the amplitude of the observations of *Wygant et al.* [2002] and of earlier observations of waves of this kind in the plasma sheet boundary layer from *Angelopoulos et al.* [1989]. Quasi-linear simulations [*Chaston et al.*, 1999b] have shown how these waves can provide electron acceleration to yield electron velocity moments of the order of half the local Alfvén speed and account for the observed wave spectra observed from the ISEE spacecraft in these regions.

9. Conclusions

[53] It has been shown that Alfvén waves are observed throughout the auroral oval from the FAST spacecraft. The cusp appears to be a region of almost permanent Alfvénic activity while the most energetic events in terms of the wave and electron energy fluxes are observed in the premidnight sector on the boundary between the statistical auroral oval and the polar cap. Electron energy fluxes in the polar cap boundary events may exceed 100 erg cm^{-2} s^{-1} (or mWm^{-2}) and thereby power the brightest aurora. Both the cusp and polar cap boundary events lie on the boundary between open and closed fieldlines suggesting magnetic reconnection at the dayside magnetopause or within the magnetotail and/or the instability of the fast flows generated in these processes as possible energy sources.

[54] Most of the electron acceleration in these waves occurs at altitudes above the FAST spacecraft from 1 to 2 R_E and is strongly dependent on variation in composition and density with altitude. The greater ionospheric scale heights together with smaller input wave energy fluxes from the magnetospheric end above the dayside auroral oval together account for the smaller energy fluxes observed here relative to those observed on the nightside. Simulations show that much of the incident wave energy is reflected from the steep Alfvén speed gradient that occurs in the transition from ionospheric to magnetospheric plasma that generally exists above FAST. For this reason it is possible that electrons accelerated by Alfvén waves above the FAST spacecraft may be observed by FAST with almost no waves present at dissipative scales. Together with the energy lost to electrons, evident in the field-aligned electron distributions, this partial reflection process accounts for the much lower wave energy fluxes observed at FAST altitudes relative to the electron energy flux.

[55] There is a decrease in wave energy flux with decreasing altitude over the FAST altitude range (350–4175 km) an order of magnitude larger than that expected from partial reflection on the Alfvén speed gradients that exist here. This suggests that much of the remaining wave energy incident from above at FAST altitudes is dissipated through wave particle interactions before reaching the ionosphere most likely through the continued acceleration of electrons (albeit much less than at altitudes above FAST) with a smaller loss through the acceleration of ions.

[56] Finally the width of the currents in these Alfvénic events as measured by the fluxgate magnetometer onboard FAST has a median value over the FAST altitude range (350–4175 km) when mapped to the ionosphere of ~1 km. If it assumed that the observed variations in each event are primarily spatial in the time it takes the FAST spacecraft to traverse them, then these widths may be related to the width of auroral features driven by these waves. With this assumption in mind the result suggests that Alfvén wave driven aurora in the ionosphere will have a distribution centered on a width of 1 km. This is consistent with the result from a study where the temporal spatial ambiguity in the observations was removed through the use of simulations [*Chaston et al.*, 2003b].

[57] **Acknowledgments.** This research was supported by NASA grants NAG5-3596 and NAG5-12453. Chris Chaston is particularly indebted to Chu Ming Chung and the Physics Department at the Chinese University of Hong Kong where much of this work was completed.

References

Allan, W., and A. Wright, Magnetotail waveguide: FAST and Alfvén waves in the plasma sheet boundary layer and lobe, *J. Geophys. Res.*, *105*, 317, 2000.

Andersson, L., J.-E. Wahlund, J. Clemmons, B. Gustavsson, and L. Eliasson, Electromagnetic waves and bursty electron acceleration: Implications from Freja, *Ann. Geophys.*, *20*, 139, 2002.

Angelopoulos, V., R. C. Elphic, S. P. Gary, and C. Y. Huang, Electromagnetic instabilities in the plasma sheet boundary layer, *J. Geophys. Res.*, *94*, 15,373, 1989.

Angelopoulos, V., J. A. Chapman, F. S. Mozer, J. D. Scudder, C. T. Russell, K. Tsuruda, T. Mukai, T. J. Hughes, and K. Yumoto, Plasma sheet electromagnetic power generation and its dissipation along auroral field lines, *J. Geophys. Res.*, *108*, doi:10.1029/2001JA900136, in press, 2003.

Berthomier, M., R. Pottelette, and A. Treumann, Parametric study of kinetic Alfvén solitons in a two electron temperature plasma, *Phys. Plasmas*, *6*, 467, 1999.

Boehm, M. H., C. W. Carlson, J. P. McFadden, J. H. Clemmons, and F. S. Mozer, High resolution sounding rocket observations of large amplitude Alfvén waves, *J. Geophys. Res.*, *95*, 12,157, 1990.

Chaston, C. C., C. W. Carlson, W. J. Peria, and R. E. Ergun, FAST observations of inertial Alfvén waves in the dayside aurora, *Geophys. Res. Lett.*, *26*, 647, 1999a.

Chaston, Y., D. Hu, and B. J. Fraser, Quasilinear evolution of the ion cyclotron beam-anisotropy instability in a current carrying plasma, *Phys. Plasmas*, *6*, 2588, 1999b.

Chaston, C. C., C. W. Carlson, and R. E. Ergun, Alfvén waves, density cavities and electron acceleration observed from the FAST spacecraft, *Phys. Scr.*, *T84*, 64, 2000a.

Chaston, C. C., Y. D. Hu, and B. J. Fraser, Quasi-linear ion cyclotron heating in the near-Earth magnetotail, *J. Geophys. Res.*, *105*, 5507, 2000b.

Chaston, C. C., W. J. Peria, C. W. Carlson, R. E. Ergun, and J. P. McFadden, FAST observations of inertial Alfvén waves and electron acceleration in the dayside aurora, *Phys. Chem. Earth*, *26*, 201, 2001.

Chaston, C. C., J. W. Bonnell, C. W. Carlson, M. Berthomier, L. M. Peticolas, I. Roth, and R. E. Ergun, Electron acceleration in the ionospheric Alfvén resonator, *J. Geophys. Res.*, *107*(A11), 1413, doi:10.1029/2002JA009272, 2002.

Chaston, C. C., J. W. Bonnell, C. W. Carlson, R. E. Ergun, and J. P. McFadden, Driven Alfvén waves and electron acceleration: A FAST case study, *Geophys. Res. Lett.*, *30*, doi:10.1029/2001GL01382, in press, 2003a.

Chaston, C. C., L. M. Peticolas, J. W. Bonnell, C. W. Carlson, and R. E. Ergun, The widths and brightness of auroral arcs driven by inertial Alfvén waves, *J. Geophys. Res.*, *108*, doi:10.1029/2001JA007537, in press, 2003b.

Chmyrev, V. M., S. V. Bilichenko, O. A. Pokhotelov, V. A. Marchenko, V. I. Lazarev, A. V. Streltsov, and L. Stenflo, Alfvén vortices and related phenomena in the ionosphere and magnetosphere, *Phys. Scr.*, *38*, 841, 1988.

Chust, T., P. Louarn, M. Volwerk, H. de Feraudy, A. Roux, J.-E. Wahlund, and B. Holback, Electric fields with large parallel component observed by the Freja spacecraft, *J. Geophys. Res.*, *103*, 215, 1998.

Dubinin, E. M., P. I. Israelevich, I. Kutiev, N. Nikolayeva, and I. Podgorny, Localised auroral disturbances as in the morning sector of the topside ionosphere as a standing electromagnetic wave, *Planet. Space Res.*, *33*, 597, 1985.

Ergun, R. E., et al., FAST satellite wave observations in the AKR source region, *Geophys. Res. Lett.*, *25*, 2061, 1998.

Gekelman, W., S. Vincena, and D. Leneman, Experimental observations of shear Alfvén waves generated by narrow current channels, *Plasma Phys. Controlled Fusion*, *39*, A101, 1997.

Goertz, C. K., and R. W. Boswell, Magnetosphere-ionosphere coupling, *J. Geophys. Res.*, *84*, 7239, 1979.

Goertz, C. K., and R. A. Smith, The thermal catastrophe model of substorms, *J. Geophys. Res.*, *94*, 6581, 1989.

Grzesiak, M., Ionospheric Alfvén resonator as seen by Freja satellite, *Geophys. Res. Lett.*, *27*, 923, 2000.

Hallinan, T., et al., Relation between optical emissions, particles, electric fields, and Alfvén waves in a multiple rayed arc, *J. Geophys. Res*, *106*, 15,445, 2001.

Hasegawa, A., Particle acceleration by MHD surface wave and formation of aurora, *J. Geophys. Res.*, *81*, 5083, 1976.

Hasegawa, A., and L. Chen, Kinetic process of plasma heating due to Alfvén wave excitation, *Phys. Rev. Lett.*, *35*, 370, 1975.

Hui, C.-H., and C. E. Seyler, Electron acceleration by Alfvén waves in the magnetosphere, *J. Geophys. Res.*, *97*, 3953, 1992.

Ivchenko, N., et al., Quasiperiodic oscillations observed at the edge of an auroral arc by Auroral Turbulence 2, *Geophys. Res. Lett.*, *26*, 3365, 1999.

Keiling, A., J. R. Wygant, C. Cattell, M. Johnson, M. Temerin, F. Mozer, C. A. Kletzing, J. Scudder, C. T. Russell, and W. Peterson, Properties of large electric fields in the plasma sheet at 4–7 Re measured with Polar, *J. Geophys. Res.*, *106*, 5779, 2001.

Kletzing, C. A., Electron acceleration by kinetic Alfvén waves, *J. Geophys. Res.*, *99*, 11,095, 1994.

Kletzing, C. A., and S. Hu, Alfvén wave generated electron time dispersion, *Geophys. Res. Lett.*, *28*, 693, 2001.

Knudsen, D. J., and J.-E. Wahlund, Core ion flux bursts within solitary kinetic Alfvén waves, *J. Geophys. Res.*, *103*, 4157, 1998.

Knudsen, D. J., M. C. Kelley, G. D. Earle, J. F. Vickrey, and M. Boehm, Distinguishing Alfvén waves from quasi-static field structures associated with discrete aurora: Sounding rocket and HILAT satellite measurements, *Geophys. Res. Lett.*, *17*, 921, 1990.

Knudsen, D. J., M. C. Kelley, and J. F. Vickrey, Alfvén waves in the auroral ionosphere: A numerical model compared with measurements, *J. Geophys. Res.*, *97*, 77, 1992.

Knudsen, D. J., J. H. Clemmons, and J.-E. Wahlund, Correlation between core ion energisation, suprathermal electron bursts and broadband ELF plasma waves, *J. Geophys. Res.*, *103*, 4171, 1998.

Knudsen, D. J., E. F. Donovan, L. L. Cogger, B. Jackel, and W. D. Shaw, Width and structure of mesoscale optical auroral arcs, *Geophys. Res. Lett.*, *28*, 705, 2001.

Koyaintsev, Y., N. Ivchenko, K. Stasiewicz, and M. Berthomier, Electron energisation by Alfvén waves: Freja and sounding rocket observations, *Phys. Scr.*, *T84*, 151, 2000.

Lessard, M. R., and D. J. Knudsen, Ionospheric reflection of small-scale Alfvén waves, *Geophys. Res. Lett.*, *28*, 3573, 2001.

Lotko, W., A. Streltsov, and C. W. Carlson, Discrete auroral arc, electrostatic shock and suprathermal electrons powered by dispersive, anomalously resistive field line resonance, *Geophys. Res. Lett.*, *25*, 4449, 1998.

Louarn, P., J.-E. Wahlund, T. Chust, H. de Feraudy, A. Roux, B. Holback, P. O. Dovner, A. I. Eriksson, and G. Holmgren, Observations of kinetic Alfvén waves by the Freja spacecraft, *Geophys. Res. Lett.*, *21*, 1847, 1994.

Lysak, R. L., Feedback instability of the ionospheric resonant cavity, *J. Geophys. Res.*, *96*, 1553, 1991.

Lysak, R. L., The relationship between electrostatic shocks and kinetic Alfvén waves, *Geophys. Res. Lett.*, *25*, 2089, 1998.

Lysak, R. L., and W. Lotko, On the kinetic dispersion relation for shear Alfvén waves, *J. Geophys. Res.*, *101*, 5085, 1996.

McFadden, J. P., C. W. Carlson, and R. E. Ergun, Microstructure of the auroral acceleration region as observed by FAST, *J. Geophys. Res.*, *104*, 14,453, 1999.

Maggs, J. E., and T. N. Davis, Measurement of the thickness of auroral structures, *Planet. Space Sci.*, *16*, 205, 1968.

Rankin, R., J. C. Samson, and V. T. Tikhonchuk, Discrete auroral arcs and nonlinear dispersive field line resonances, *Geophys. Res. Lett.*, *26*, 663, 1999.

Seyler, C. E., A mathematical model of the structure and evolution of small scale discrete auroral arcs, *J. Geophys. Res.*, *95*, 17,199, 1990.

Seyler, C. E., A. E. Clark, J. Bonnell, and J.-E. Wahlund, Electrostatic broadband ELF wave emission by Alfvén wave breaking, *J. Geophys. Res.*, *103*, 7027, 1998.

Shay, M. A., J. F. Drake, B. N. Rogers, and R. E. Denton, Alfvénic collisionless magnetic reconnection and the Hall term, *J. Geophys. Res.*, *106*, 3759, 2001.

Stasiewicz, K., et al., Small scale Alfvénic structure in the aurora, *Space Sci. Rev.*, *92*, 423, 2000.

Strangeway, R. J., et al., FAST observations of VLF waves in the auroral zone: Evidence of very low plasma densities, *Geophys. Res. Lett.*, *25*, 2065, 1998.

Thompson, B. J., and R. L. Lysak, Electron acceleration by inertial Alfvén waves, *J. Geophys. Res.*, *101*, 5359, 1996.

Trondsen, T. S., L. L. Cogger, and J. C. Samson, Asymmetric multiple auroral arcs and inertial Alfvén waves, *Geophys. Res. Lett.*, *24*, 2945, 1997.

Tung, Y.-K., C. W. Carlson, J. P. McFadden, D. M. Klumpar, G. K. Parks, W. J. Peria, and K. Liou, Auroral polar cap boundary ion conic outflow observed on FAST, *J. Geophys. Res.*, *106*, 3603, 2001.

Volwerk, M., P. Louarn, T. Chust, A. Roux, H. de Feraudy, and B. Holback, Solitary kinetic Alfvén waves: A study of the Poynting flux, *J. Geophys. Res.*, *101*, 13,335, 1996.

Wahlund, J.-E., et al., On ion acoustic turbulence and the non-linear evolution of kinetic Alfvén waves in the aurora, *Geophys. Res. Lett.*, *21*, 1831, 1994.

Wahlund, J.-E., et al., Broadband ELF plasma emission during auroral energisation, 1, Slow ion acoustic waves, *J. Geophys. Res.*, *103*, 4343, 1998.

Wygant, J. R., et al., Polar spacecraft based comparisons of intense electric fields and Poynting flux near and within the plasma sheet tail lobe boundary to UVI images: An energy source for the aurora, *J. Geophys. Res.*, *105*, 18,675, 2000.

Wygant, J. R., et al., Evidence for kinetic Alfvén waves and parallel electron energization at 4–6 Re altitudes in the plasma sheet boundary layer, *J. Geophys. Res.*, *107*(A8), 1201, doi:10.1029/2001JA900113, 2002.

J. W. Bonnell, C. W. Carlson, C. C. Chaston, and J. P. McFadden, Space Sciences Laboratory, University of California, Berkeley, CA 94720, USA. (ccc@ssl.berkeley.edu)

R. E. Ergun, Laboratory for Atmospheric and Space Physics, University of Colorado, Boulder, CO 80309, USA. (ree@fast.colorado.edu)

R. J. Strangeway, Institute for Geophysics and Planetary Physics, University of California, Los Angeles, CA 90024, USA. (strangeway@igpp.ucla.edu)